Article

Structural Development of Mercaptophenol Self-Assembled Monolayers and the Overlying Mineral Phase during Templated CaCO Crystallization from a Transient Amorphous Film

Jonathan R. I. Lee, T. Yong-Jin Han, Trevor M. Willey, Dongbo Wang, Robert W. Meulenberg, Joakim Nilsson, Patricia M. Dove, Louis J. Terminello, Tony van Buuren, and James J. De Yoreo

J. Am. Chem. Soc., **2007**, 129 (34), 10370-10381• DOI: 10.1021/ja071535w • Publication Date (Web): 02 August 2007

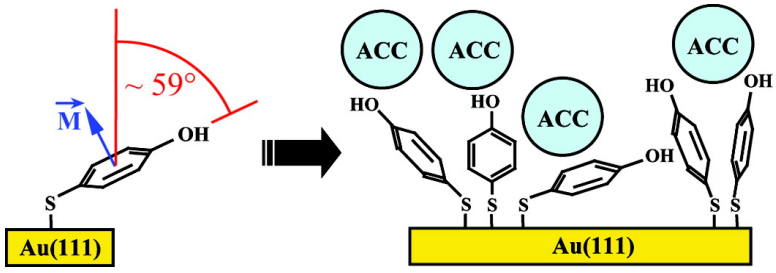

More About This Article

Additional resources and features associated with this article are available within the HTML version:

- Supporting Information
- Links to the 10 articles that cite this article, as of the time of this article download
- Access to high resolution figures
- Links to articles and content related to this article
- Copyright permission to reproduce figures and/or text from this article

View the Full Text HTML

J|A|C|S
ARTICLES
Published on Web 08/02/2007

Structural Development of Mercaptophenol Self-Assembled Monolayers and the Overlying Mineral Phase during Templated $CaCO_3$ Crystallization from a Transient Amorphous Film

Jonathan R. I. Lee,*,† T. Yong-Jin Han,† Trevor M. Willey,† Dongbo Wang,‡ Robert W. Meulenberg,† Joakim Nilsson,† Patricia M. Dove,‡ Louis J. Terminello,† Tony van Buuren,† and James J. De Yoreo*,†

Contribution from the Lawrence Livermore National Laboratory, Livermore, California 94550, and Virginia Tech, Blacksburg, Virginia 24061

Received March 5, 2007; E-mail: lee204@llnl.gov; deyoreo1@llnl.gov

Abstract: Formation of biomineral structures is increasingly attributed to directed growth of a mineral phase from an amorphous precursor on an organic matrix. While many in vitro studies have used calcite formation on organothiol self-assembled monolayers (SAMs) as a model system to investigate this process, they have generally focused on the stability of amorphous calcium carbonate (ACC) or maximizing control over the order of the final mineral phase. Little is known about the early stages of mineral formation, particularly the structural evolution of the SAM and mineral. Here we use near-edge X-ray absorption spectroscopy (NEXAFS), photoemission spectroscopy (PES), X-ray diffraction (XRD), and scanning electron microscopy (SEM) to address this gap in knowledge by examining the changes in order and bonding of mercaptophenol (MP) SAMs on Au(111) during the initial stages of mineral formation as well as the mechanism of ACC to calcite transformation during template-directed crystallization. We demonstrate that formation of ACC on the MP SAMs brings about a profound change in the morphology of the monolayers: although the as-prepared MP SAMs are composed of monomers with well-defined orientations, precipitation of the amorphous mineral phase results in substantial structural disorder within the monolayers. Significantly, a preferential face of nucleation is observed for crystallization of calcite from ACC on the SAM surfaces despite this static disorder.

1. Introduction

The observation of oriented crystals in a wide variety of biomineralized structures has motivated numerous investigations into template-directed nucleation and growth of crystals by organic or macromolecular films. Most studies have focused on calcite, which is ubiquitous among biominerals formed by marine organisms. Some researchers—notably Addadi, Wiener, and co-workers—used mimics of biomineralizing frameworks from such organisms[1−4] to explore templating, but other laboratory studies primarily utilized highly idealized surfaces, particularly Langmuir monolayers at air−water interfaces[5−15] and self-assembled monolayers (SAMs) on noble-metal surfaces.[16−24] These investigations generally sought to explore film and/or substrate parameters leading to the highest degree of control over crystal orientation. They have been used to

† Lawrence Livermore National Laboratory.
‡ Virginia Tech.

(1) Aizenberg, J.; Lambert, G.; Weiner, S.; Addadi, L. *J. Am. Chem. Soc.* **2002**, *124*, 32.
(2) Raz, S.; Hamilton, P. C.; Wilt, F. H.; Weiner, S.; Addadi, L. *Adv. Funct. Mater.* **2003**, *13*, 480.
(3) Addadi, L.; Raz, S.; Weiner, S. *Adv. Mater.* **2003**, *15*, 959.
(4) Addadi, L.; Joester, D.; Nudelman, F.; Weiner, S. *Chem. Eur. J.* **2006**, *12*, 980.
(5) Mann, S.; Heywood, B. R.; Rajam, S.; Birchall, J. D. *Nature* **1988**, *334*, 692.
(6) Mann, S.; Heywood, B. R.; Rajam, S.; Walker, J. B. A. *J. Phys. D: Appl. Phys* **1991**, *154*.
(7) Walker, J. B. A.; Heywood, B. R.; Mann, S. *J. Mater. Chem.* **1991**, *1*, 889.
(8) Heywood, B. R.; Rajam, S.; Mann, S. *J. Chem. Soc., Faraday Trans.* **1991**, *87*, 735.
(9) Rajam, S.; Heywood, B. R.; Walker J. B. A.; Mann, S.; Davey, R. J.; Birchall, J. D. *J. Chem. Soc., Faraday Trans.* **1991**, *87*, 727.
(10) Mann, S.; Archibald, D. D.; Didymus, J. M.; Douglas, T.; Heywood, B. R.; Meldrum, F. C.; Reeves, N. J. *Science* **1993**, *261*, 1286.
(11) Heywood, B. R.; Mann, S. *Chem. Mater.* **1994**, *6*, 311.
(12) Litvin, A. L.; Valiyaveettil, S.; Kaplan, D. L.; Mann, S. *Adv. Mater.* **1997**, *9*, 124.
(13) Buijnsters, P. J. J. A.; Donners, J. J. J. M.; Hill, S. J.; Heywood, B. R.; Nolte, R. J. M.; Zwanenburg, B.; Sommerdijk, N. A. J. M. *Langmuir* **2001**, *17*, 3623.
(14) Loste, E.; Diaz-Martí, E.; Zarbakhsh, A.; Meldrum, F. C. *Langmuir* **2003**, *19*, 2830.
(15) Volkmer, D.; Fricke, M.; Gleiche, M.; Chi, L. *Mater. Sci. Eng. C* **2005**, *25*, 161.
(16) Aizenberg, J.; Black, A. J.; Whitesides, G. M. *J. Am. Chem. Soc.* **1999**, 4500.
(17) Aizenberg, J. *J. Cryst. Growth* **2000**, *143*, 28
(18) Travaille, A. M.; Donners, J. J. J. M.; Gerritsen, J. W.; Sommerdijk, N. A. J. M.; Nolte, R. J. M.; van Kempen, H. *Adv. Mater.* **2002**, *14*, 492.
(19) Travaille, A. M.; Kaptijn, L.; Verwer, P.; Hulsken, B.; Elemans, J. A. A. W.; Nolte, R. J. M.; van Kempen, H. *J. Am. Chem. Soc.* **2003**, *125*, 11571.
(20) Han, Y. J.; Aizenberg, J. *Angew. Chem., Int. Ed.* **2003**, 3668.
(21) Aizenberg, J.; Muller, D. A.; Grazul, J. L.; Hamann, D. R. *Science* **2003**, *299*, 1205.
(22) Aizenberg, J. *Adv. Mater.* **2004**, *16*, 1295.
(23) Han, Y. J.; Wysocki, L. M.; Thanawala, M. S.; Siegrist, T.; Aizenberg, J. *Angew. Chem., Int. Ed.* **2005**, *44*, 2386.
(24) Kwak, S. Y.; DiMasi, E.; Han, Y.-J.; Aizenberg, J.; Kuzmenko, I. *J. Cryst. Growth Des.* **2005**, *5*, 2139.

10.1021/ja071535w CCC: $37.00

deduce structural relationships between templating surfaces and nucleating crystals by comparing the packing geometry of well-ordered monolayers to the molecular structure of the apparent plane of nucleation. At least one study attempted to probe the thermodynamic drivers behind crystal templating at carboxyl-terminated SAMs on Au.[25]

In nearly all of these studies the final crystal phase and orientation as well as the structure of the well-ordered SAM were assumed to define the structural state of the crystal nucleus and film at the time of nucleation. In contrast, the pathways of templated crystallization, particularly the structural coevolution of both monolayer and mineral phase, have received little attention. The importance of performing such studies is highlighted by recent findings that show or strongly suggest that many calcitic biomineral structures do not grow directly from solution but transform from a precursor phase of amorphous calcium carbonate (ACC),[3,26−31] which is stabilized (to exhibit a prolonged lifetime) either by soluble proteins within the ACC or by a surrounding matrix. Numerous experiments have shown that ACC can also be stabilized in the laboratory using poly(aspartic acid)[32] or poly(acrylic acid) (PAA)[33−36] in solution. Alternatively, deposition from a highly supersaturated solution onto an OH-terminated film can be used to produce a transient ACC phase.[37] Although one study probed the kinetics of PAA-stabilized ACC formation and transformation at the surface of organothiol SAMs[24] and another looked at mineral and film evolution on Langmuir monolayers at an air−water interface,[33] here again most investigations examined the parameters that maximize control over ACC formation rather than considering the dynamics of the transformation itself. Consequently, the thermodynamic, structural, and kinetic controls on both templating and the ACC to calcite transformation remain poorly understood.

Three fundamental questions about these processes need to be addressed: (1) What is the structural relationship between the film and mineral during the nucleation phase of mineral formation; (2) What pathway through the potential cascade of metastable phases does the system follow in going from the solvated state through the ACC phase to the final calcitic state; and (3) What are the interfacial energies and kinetic barriers associated with these processes? The purpose of this study is to begin to address these questions by combining the ability of hydroxyl-terminated films on Au to transiently stabilize ACC in the absence of additives with the capacity of synchrotron-based techniques, near-edge X-ray absorption fine structure (NEXAFS) spectroscopy, and photoemission spectroscopy (PES), to provide detailed information about monolayer structure and bonding. Specifically, we present results on the evolution of SAM monomer orientation during the process of ACC precipitation from solution, document the mode of transformation to calcite, and determine the degree of crystal order that arises upon transformation.

The work described here was performed using SAMs prepared from three structural isomers of a hydroxyl-terminated organothiol: 2-, 3-, and 4-mercaptophenol (MP), of which the latter has recently been employed in the functionalization of Au colloids for novel crystallization strategies.[38] Selection of these isomers, rather than the OH-terminated alkanethiols used almost exclusively in previous studies of monolayer-mediated mineral nucleation and growth,[6,16,23,37] is significant for several reasons. First, MP monomers present the hydroxyl functionality required for stabilization of ACC over the time frame (hours) required for NEXAFS and PES measurements. Second, since MP SAMs with well-defined molecular orientation can be made from all three isomers, each of which presents a unique OH configuration, they provide internal controls on the role of SAM chemistry and structure in directing crystal templating. Finally, each MP monomer contains an aryl ring, which allows us to utilize angular dependent NEXAFS spectroscopy to quantify the molecular orientation of the MP molecules in the SAM, even in the presence of an ACC precipitate.

Our measurements lead to four significant observations: (1) Although all of the SAMs initially exhibit well-defined molecular orientations, subsequent exposure to the aqueous environments required to induce ACC precipitation causes the monolayers to disorder. (2) Under the conditions typically used for these kinds of experiments, ACC forms in solution and then precipitates onto the monolayer. (3) Over time the ACC precipitate, which is comprised of spherical particles < 100 nm in diameter covering about 65% of the SAM surface, transforms into discrete crystals that are predominantly calcite (80%) accompanied by a small proportion of vaterite (20%). However, this does not occur through direct ACC dehydration or solid-state transformation but via a dissolution−reprecipitation reaction. (4) Despite the extensive disordering of the monolayer that occurs during the course of the initial ACC precipitation, the resulting calcite crystals display a high degree of orientational uniformity on the 3- and 4-MP surfaces where the (104) face defines the apparent plane of nucleation but show no such uniformity on the 2-MP surface. Moreover, comparison with negative and positive control experiments on bare Au and OH-terminated Ag and silica surfaces shows that the SAMs are essential for bringing about the observed (104) face-selective nucleation.

These observations lead us to conclude that, for the MP/$CaCO_3$ systems, the view of calcite templating in which a well-ordered organic film induces surface nucleation of oriented calcite directly from solution on a crystal plane whose molecular structure is matched to that of the film fails to capture the complex dynamics that precede the final, well-ordered product. Rather, even in the absence of stabilizers, the first phase to form is ACC. Whether or not one of the ACC particles then serves as the initiator for calcite formation, the overwhelming source of nutrient for the growing crystals comes from dissolution of this amorphous solute reservoir. Finally, the organic film

(25) Travaille, A. M.; Steijven, E. G. A.; Meekes, H.; van Kempen, H. *J. Phys. Chem. B* **2005**, *109*, 5618.
(26) Lowenstam, H. A. *Science* **1981**, *211*, 1126.
(27) Weiss, I. M.; Tuross, N.; Addadi, L.; Weiner, S. *J. Exp. Zool.* **2002**, *293*, 478.
(28) Cölfen, H.; Mann, S. *Angew. Chem., Int. Ed.* **2003**, *42*, 2350.
(29) Politi, Y.; Arad, T.; Klein, E.; Weiner, S.; Addadi, L. *Science* **2004**, *306*, 1161.
(30) Weiner, S.; Sagi, I.; Addadi, L. *Science* **2005**, *309*, 1027.
(31) Politi, Y.; Levi-Kalisman, Y.; Raz, S.; Wilt, F.; Addadi, L.; Weiner, S.; Sagi, I. *Adv. Funct. Mater.* **2006**, *16*, 1289.
(32) Cheng, X.; Gower, L. B. *Biotechnol. Prog.* **2006**, *22*, 141.
(33) DiMasi, E.; Kwak, S.-Y.; Amos, F. F.; Olszta, M. J.; Lush, D.; Gower, L. B. *Phys. Rev. Lett.* **2006**, *97*, 045503.
(34) Olszta, M. J.; Gajjeraman, S.; Kaufman, M.; Gower, L. B. *Chem. Mater.* **2004**, *16*, 2355.
(35) Xu, X.; Han, J. T.; Cho, K. *Chem. Mater.* **2004**, *16*, 1740.
(36) Xu, G.; Yao, N.; Aksay, I. A.; Groves, J. T. *J. Am. Chem. Soc.* **1998**, *120*, 11977.
(37) Han, Y. J.; Aizenberg, J. *Mater. Res. Soc. Symp. Proc. 873E* **2005**, K4.10.129
(38) Küther, J.; Seshadri, R.; Tremel, W. *Angew. Chem., Int. Ed.* **1998**, *37*, 3044.

apparently does not need to be well ordered to induce oriented growth because either (1) the chemistry of the SAM surface simply favors growth on the crystal plane for which the interfacial energy is lowest, (2) small (nanometer scale) regions of SAM monomers retaining order are large enough to still direct the orientation of the initial seed crystals, or (3) the ability of the monomers to reorder allows the crystal and film to template one another during the transformation from ACC to calcite. Of course, there are many important subtleties associated with these conclusions, and we consider them within the discussion of our results.

2. Experimental Section

Reagents and Materials. All reagents were obtained from commercial sources and used as received. 4-Mercaptophenol (97%), 3-mercaptophenol (96%), and 2-mercaptophenol (95%) were purchased from Aldrich. Ethanol (200% proof) was purchased from Aaper. Ammonium carbonate (99.999%) was purchased from Alfa Aesar. Calcium chloride dihydrate (99.5%) was obtained from EMD Chemicals. Au(111) samples were prepared under high vacuum by thermal evaporation of 5 nm of Ti (99.99%, VWR) and then 100 nm of Au (99.99%, VWR) onto Si(100). All Au(111) samples were hydrogen flame annealed immediately prior to use following well-established experimental protocols.[39]

Sample Preparation. To prepare the MP SAMs freshly annealed Au(111) samples were immersed in 1−2 mM ethanolic solutions of the required MP isomer for a period of 24−36 h. Upon emersion the samples were immediately rinsed with pure ethanol solvent, dried in a diffuse stream of N_2, and transferred to either ultrahigh vacuum (UHV) for NEXAFS and PES measurements or 10 mM aqueous (deionized water, 18.2 MΩ, Milli-Q) solutions of calcium chloride in preparation for $CaCO_3$ growth. All MP SAMs on Au(111) were generated under the same ambient conditions.

Precipitation of ACC and subsequent growth of crystalline $CaCO_3$ on the MP SAMs was conducted using a CO_2 diffusion method following experimental procedures described in the literature.[20] MP SAM samples immersed in individual solutions of calcium chloride were transferred to a sealed desiccator in which they were exposed to CO_2 vapor from decomposition of $(NH_4)_2CO_3$. Upon formation of the desired phase (either ACC or, following longer periods of exposure, the crystalline mineral) and surface coverage of $CaCO_3$, the samples were removed from the desiccator, rinsed with acetone, and dried in a diffuse stream of N_2. An identical procedure was used to induce $CaCO_3$ crystallization on annealed Au(111) and glass substrates, which served as experimental controls. ACC precipitate formed on the MP SAMs was stable in air for ∼5 days. Nevertheless, all ACC on MP SAM samples were transferred to the NEXAFS/PES UHV chamber within 90 min of preparation in order to minimize any degradation of the organic monolayer.

Instrumentation. X-ray absorption and X-ray photoemission spectra were recorded on VUV BL8.2 of the Stanford Synchrotron Radiation Laboratory (SSRL, SPEAR III) at the Stanford Linear Accelerator (SLAC). SSRL is operated with a storage ring energy of 3 GeV and beam current of approximately 100 mA. BL8.2 offers an energy resolution of ∼0.2 eV at the carbon *K* edge, and the cross section of the focused beam was ∼1 mm in diameter at the sample surface. NEXAFS spectra were recorded in the total electron yield (TEY) mode. The TEY signal was obtained by measuring the total current leaving the experimental sample as the energy was scanned across the absorption edge. All NEXAFS and PES signals were normalized to the I_0 current, which was recorded for the incident X-ray beam via a freshly coated Au grid located upstream of the experimental sample. The degree of linear polarization, *P*, in the incident beam was determined prior to each series of NEXAFS experiments using established protocols reported in the literature.[40,41] The calculated polarization was 99% in the plane of the storage ring throughout the course of the experiments described in this manuscript. For carbon NEXAFS measurements, the energy scale on BL8.2 was calibrated to the C(1s) → π^* resonance for a freshly cleaved sample of highly oriented pyrolytic graphite to which an energy of 285.38 eV was assigned.[42] All NEXAFS and PES measurements were conducted at base pressures of $\leq 1 \times 10^{-9}$ Torr. Care was taken to minimize beam damage of the MP and MP/ACC samples when conducting NEXAFS and PES measurements.[43] Each spectrum was recorded from a fresh region of the sample surface, and beam exposure during data collection was limited to the time frame required for good signal-to-noise statistics. For carbon *K*-edge NEXAFS, which were collected over a spectral range of 280−330 eV, this corresponded to ∼5 min per spectrum. In comparison, a period of only ∼3 min was required for each PES spectrum, irrespective of the element of interest.

All PES data was recorded using a PHI15-255G cylindrical mirror analyzer, which was operated at a pass energy of 25 eV. C(1s) spectra were obtained at an incident photon energy of 400 eV; S(2p) spectra were obtained at incident photon energies of 280 and 400 eV. For purposes of energy calibration, a PES spectrum of the Au(4f) electrons was recorded immediately after each C(1s) and S(2p) measurement on the same region of the sample surface. The Au($4f_{7/2}$) photoelectron at 84.01 ± 0.05 eV was then used to convert from kinetic energy to binding energy scales. All contact angle measurements were conducted in a static sessile drop mode using a Krüss G10 analysis system with DSA1 software. XRD spectra were collected over a $10° \leq 2\theta \leq 60°$ range using a PEI vertical goniometer and Cu Kα radiation. The XRD spectrum collected from a flame-annealed Au(111) on Si(100) reference was used to subtract substrate reflections from samples supporting crystalline $CaCO_3$. Scanning electron microscopy (SEM) images were collected along the Au(111) surface normal using a Hitachi S-800 scanning electron microscope.

NEXAFS Analysis. NEXAFS yields a quantitative assignment of bond orientation through analysis of the angular dependencies of various resonances. As such, one can use the technique to determine monomer orientation within the MP SAMs both before and after ACC formation. The intensity of any NEXAFS resonance is proportional to the dot product between the transition dipole moment (TDM) of an unoccupied orbital and the electric field vector of the incident X-ray beam. For MP SAMs prepared on Au(111), the TDM can be modeled as a vector for the π^* orbital of the aryl ring present in each monomer. This vector lies perpendicular to the plane of each MP isomer. For resonances modeled by a vector TDM, the intensity, I_v, is expressed as[44,45]

(39) Hydrogen flame annealing follows the method described by Molecular Imaging, Inc. in http://www.molec.com/anneal.html (accessed Sept 2006).

(40) Willey, T. M.; Vance, A. L.; van Buuren, T.; Bostedt, C.; Nelson, A. J.; Terminello, L. J.; Fadley, C. S. *Langmuir* **2004**, *20*, 2746.
(41) Lee, J. R. I.; Willey, T. M.; Nilsson, J.; Terminello, L. J.; De Yoreo, J. J.; van Buuren, T. *Langmuir* **2006**, *22*, 11134.
(42) Batson, P. E. *Phys. Rev. B* **1993**, *48*, 2608.
(43) Zharnikov, M.; Grunze, M. *J. Vac. Sci. Technol. B* **2002**, *20*, 1793.
(44) Stöhr, J.; Outka, D. A. *Phys. Rev. B* **1987**, *36*, 7891.
(45) Stöhr, J. *NEXAFS Spectroscopy*; Springer-Verlag: New York, 1992.
(46) Bagus, P. S.; Weiss, K.; Schertel, A.; Wöll, C.; Braun, W.; Hellwig, C.; Jung, C. *Chem. Phys. Lett.* **1996**, *248*, 129.
(47) Chattopadhyay, S.; Brahma, S. K. *Spectrochim. Acta, Part A* **1993**, *49*, 589.
(48) Castner, D. G.; Hinds, K.; Grainger, D. W. *Langmuir* **1996**, *12*, 5083.
(49) Lamont, C. L. A.; Wilkes, J. *Langmuir* **1999**, *15*, 2037.
(50) Calculation of X-ray attenuation lengths was conducted using the program available in http://www-cxro.lbl.gov/optical constants/atten2.html (accessed Dec 2006).
(51) Ohara, H.; Yamamoto, Y.; Kajikawa, K.; Ishii, H.; Seki, K.; Ouchi, Y. *J. Synchrotron Rad.* **1999**, *6*, 803.
(52) Zharnikov, M.; Frey, S.; Heister, K.; Grunze, M. J. *Electron Spectrosc. Relat. Phenom.* **2002**, *124*, 15.
(53) Brecevic, L.; Nielsen, A. E. *J. Cryst. Growth* **1989**, *98*, 504.

$$I_v(\theta,\alpha) \propto \frac{1}{3}P\left[1 + \frac{1}{2}(3\cos^2\alpha - 1)(3\cos^2\theta - 1)\right] + \frac{1}{2}(1 - P)\sin^2\alpha \quad (1)$$

where θ represents the angle between the incident radiation and the surface ($\leq 90°$) and α represents the angle between the TDM vector, $\vec{M}$, and the surface normal. For the C−C and C−O σ^* orbitals and the Rydberg (R^*) [46]/C−H σ^* resonances, the TDM is modeled by a plane, which is coincident with the plane of the aryl ring in MP. In this instance, the resonance intensity I_p is expressed as[44,45]

$$I_p(\theta,\gamma) \propto \frac{2}{3}P\left[1 - \frac{1}{4}(3\cos^2\theta - 1)(3\cos^2\gamma - 1)\right] + \frac{1}{2}(1 - P)(1 + \cos^2\gamma) \quad (2)$$

where γ represents the angle between the surface normal and the normal to the plane of the TDM. To remove the proportionality, ratios are taken between spectra recorded at different angles of incidence. In order to simplify analysis, the intensities are left as functions of cosine squared. With $\Theta = \cos^2\theta$, $A = \cos^2\alpha$, and $\Gamma = \cos^2\gamma$, the intensities from eqs 1 and 2 become

$$\frac{I_v(\Theta_i,A)}{I_v(\Theta_j,A)} = \frac{P(3A - 1)\Theta_i - A + 1}{P(3A - 1)\Theta_j - A + 1} \quad (3)$$

and

$$\frac{I_p(\Theta_i,\Gamma)}{I_p(\Theta_j,\Gamma)} = \frac{P(3\Gamma - 1)\Theta_i - \Gamma - 1}{P(3\Gamma - 1)\Theta_j - \Gamma - 1} \quad (4)$$

respectively. These two equations are linear in Θ_i. A linear regression is obtained from all spectra acquired at Θ_i versus all spectra acquired at Θ_j, which allows α and γ to be solved as a function of the slopes or offsets. In principle, a high degree of precision, $<\pm 1°$, is possible from regression analysis on spectra recorded at multiple angles of incidence. Nevertheless, several additional sources of systematic error are omitted from this estimate, and the predicted accuracy is actually closer to $\pm 4-5°$.

3. Results

3.1. Morphology and Bonding within MP SAMs Prior to $CaCO_3$ Formation. To address the structural development of the MP SAMs with $CaCO_3$ formation, it was necessary to first characterize the structure and bonding of the monolayers before ACC precipitation. In this section, we demonstrate that the as-prepared MP SAMs are predominantly composed of monomers with well-defined orientation that are bonded to the underlying Au(111) substrate via an Au−thiolate bond. NEXAFS spectroscopy, PES, and contact angle measurements were used for this purpose.

Figure 1a, b, and c displays representative carbon *K*-edge NEXAFS spectra recorded for SAMs prepared on Au(111) from ethanolic solutions of 2-, 3-, and 4-MP, respectively. The spectra were collected for a range of angles of incidence between the axis of the X-ray beam and the surface of the experimental sample within the limits of normal (90°) and approaching grazing (20°) incidence. Each of the NEXAFS signals presented in the upper panels of Figure 1a−c was obtained by normalizing the raw data to both the I_0 current and the absorption edge step. The magnitude of this step is defined as the difference in absorption signal between the preedge (280 eV) and immediately postedge (325 eV) regions. The lower panels of Figure 1a−c contain difference spectra obtained by subtraction of the 20° scan from spectra recorded at each of the other angles of incidence. Large features in the difference spectra are indicative of angular dependence in the orbital responsible for the NEXAFS resonance and, therefore, of well-defined bond/functional group orientation. Moreover, a preliminary assignment of this bond orientation can be inferred from inspection of the direction of these difference features. For the experimental geometry employed in this study, features pointing downward in the difference spectra indicate that the TDM vector is oriented between the Au(111) surface normal and the magic angle ($\arcsin[(2/3)^{1/2}]$, ~54.7°, from the surface normal). Equally, features directed upward denote that the TDM vector is aligned more closely with the surface plane, oriented at least 54.7° from the surface normal.

A series of pronounced NEXAFS resonances are observed in Figure 1a−c. Each normalized NEXAFS spectrum displays a peak at 285.3 eV, which is assigned to π^* transitions for the five aryl carbons in MP that are not bonded to oxygen. In addition, a shoulder to the resonance is resolved at 285.8 eV. These features are attributed to differences in the C(1s) orbital energies that arise from variation in the relative through-bond proximities of the aryl carbons to the electron-withdrawing hydroxyl oxygen. The resonance observed at 287.1 eV corresponds to the π^* transition for the aryl carbon bonded to the hydroxyl group. It appears at a higher incident photon energy than the alternative aryl carbon resonances due to the strong inductive effect of the hydroxyl oxygen and is convoluted with an unresolved C−S σ^* resonance at ~287 eV.[44] The spectral feature at 288.6 eV is attributed to C−H σ^*/R* transitions. Two broad peaks are also evident at 294.2 and 302.6 eV, which arise due to C(1s) → C−C σ^* transitions.[40,44]

The aryl carbon π^* resonances demonstrate strong angular dependence in the NEXAFS spectra recorded for SAMs prepared on Au(111) from each isomer of MP. Therefore, the monomers adopt well-defined molecular orientations within their respective monolayers. Given that the π^* resonances exhibit greater intensities at grazing than normal beam incidence in Figure 1a−c, the corresponding TDM vectors must be oriented within 54.7° of the Au(111) surface normal for each isomer of MP. By extension, one can conclude that monomers of 2-, 3-, and 4-MP all adopt an orientation on Au(111) that is more prostrate than upright because the π^* TDM vectors are perpendicular to the plane of the aryl ring (Figure 2).

Linear regression analysis of the π^* resonance intensities provides a more quantitative measurement of molecular orientation within the MP SAMs. Table 1 contains the tilt (colatitudal) angle obtained for the plane of each MP isomer with respect to the Au(111) surface normal via analysis of the 285.3 eV π^* resonance intensities. We note, however, that in the assignment of singular tilt angles for 2-, 3-, and 4-MP one must also define the twist (dihedral) angle of the monomers about the axis coincident with the C−S σ bond (Figure 3). This criterion arises due to restrictions of the experimental geometry, which allow only for measurement of the interdependency between the tilt and the twist angles during regression analysis of the NEXAFS resonances. The tilt angles presented in Table 1 were obtained for a twist angle of 0°, i.e., directly from the polar angle of the π^* TDM vector. Extended linear regression analysis (see Supporting Information) indicates, however, that there is limited

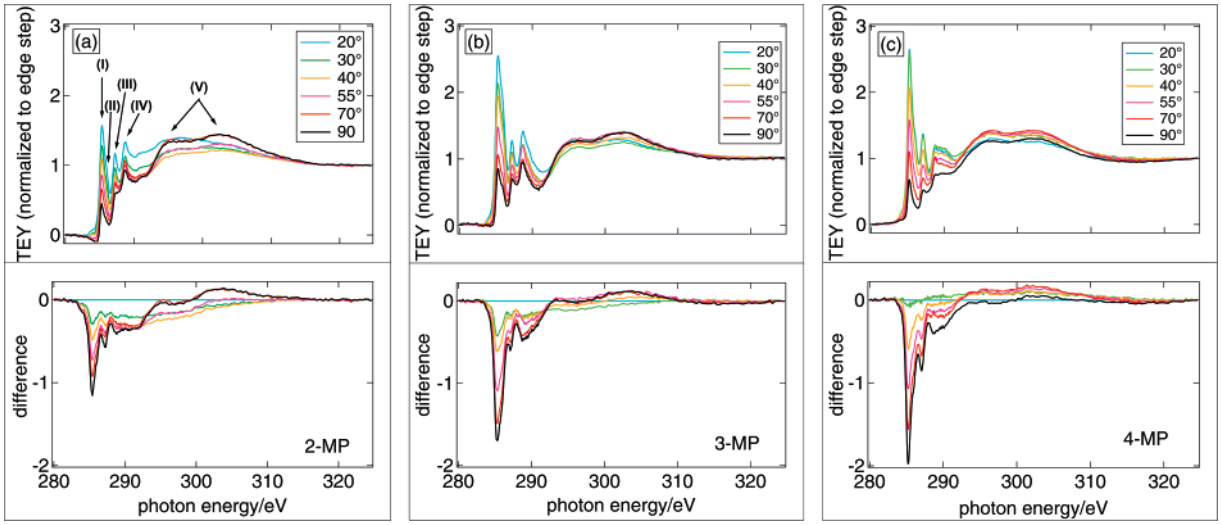

Figure 1. Normalized carbon *K*-edge NEXAFS spectra recorded in the TEY mode for (a) 2-MP, (b) 3-MP, and (c) 4-MP SAMs prepared on Au(111) from pure EtOH solvent. The peaks observed in the NEXAFS spectra correspond to the following resonances: (I) the π^* transitions for the five aryl carbons in MP that are not bonded to oxygen, (II) a shoulder to I that is also attributed to the π^* transitions for these five aryl carbons, (III) the π^* transition for the aryl carbon bonded to the hydroxyl group, (IV) the C−H σ^*/R* transitions, and (V) the C−C σ^* transitions.

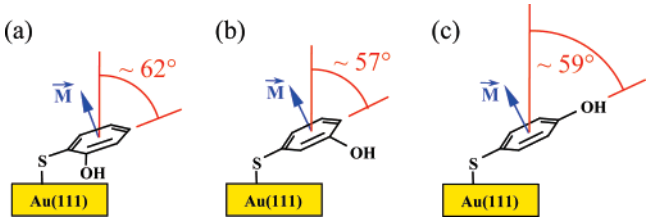

Figure 2. Schematic indicating the molecular tilt angles for (a) 2-MP, (b) 3-MP, and (c) 4-MP in their respective SAMs on Au(111). The transition dipole moment vector for the extended π system of each molecule is included for clarity. All of the tilt angles were obtained under the assumption of 0° twist about the C−S σ bond.

Table 1. Colatitudal Tilt Angles and Integrated S(2p) PES Resonances for SAMs of Each Isomer of MP on Au(111) and SAMs of 3- and 4-MP Supporting ACC Precipitate[a]

	tilt angle (deg)	elemental sulfur (%)	bound thiolate (%)	unbound mercaptan (%)	contact angle (deg)
2-MP	61	16 ± 4	75 ± 6	9 ± 6	51
3-MP	59	12 ± 5	71 ± 3	15 ± 6	45
4-MP	57	9 ± 5	76 ± 3	12 ± 5	24
3-MP/ACC	disordered (38)	19 ± 4	56 ± 2	18 ± 6	
4-MP/ACC	disordered (35)	21 ± 6	59 ± 4	15 ± 5	

[a] Contact angles with water are also included for monolayers of each isomer of MP. The tilt angles have an accuracy of ±4−5%, and the contact angles have an accuracy of ±2−3°.

variation in the tilt angle (<10°) as a function of molecular rotation about the C−S σ bond. As a consequence, the tilt angles calculated for a twist of 0° are representative and provide an excellent measure of molecular orientation.

The averaged tilt angles obtained for monomers of 2-, 3-, and 4-MP reside within experimental error of one another and are all on the order of ∼60° from the Au(111) surface normal (Figure 2). Such strong similarity suggests that the SAMs of each MP isomer contain comparable bonding interactions and interadsorbate packing. Analysis of the carbon *K*-edge NEXAFS in isolation does not allow for a definitive assignment of the molecular packing within the MP monolayers. Nonetheless, one can exclude the possibility of any interaction between the π system of the aryl ring and the underlying substrate comparable

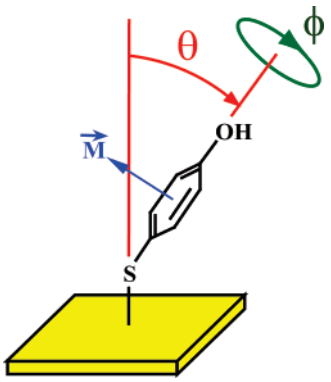

Figure 3. Schematic demonstrating the tilt, θ, and twist, ϕ, angles for 4-MP on an Au substrate. The tilt angle corresponds to the angle between the surface normal and the axis coincident with the C−S σ bond. The twist angle corresponds to the degree to which the molecule is rotated about the axis of the C−S σ bond.

to the bonding proposed for isonicotinic acid, a close structural analogue of MP, on Ag sol.[47] An interaction of this kind would offer an explanation for the three isomers of MP adopting comparable tilt angles but is inconsistent with the specific tilt angles measured in this study because it would require a more prostrate orientation of the aryl ring with respect to the Au(111) surface.

Additional characterization of the bonding within the MP SAMs was conducted via PES. Figure 4 displays representative S(2p) PES spectra recorded for monolayers of MP prepared on Au(111). The accompanying best-fit model spectra are comprised of four separate S(2p) resonances that each correspond to a specific sulfur environment near the substrate surface. All of the resonances are spin−orbit split into doublets with a branching ratio of ∼2:1 and an energy separation of ∼1.2 eV. The S $2p_{3/2}$ (S $2p_{1/2}$) resonance observed at the lowest binding energy, 160.8 eV (162.0 eV), is attributed to 'elemental' sulfur. The subsequent resonance at 161.9 eV (163.1 eV) corresponds to 'bound' monomers of MP, which are attached to the underlying substrate via an Au−thiolate bond (Figure 5).[48] 'Unbound' monomers retain their mercaptan group (−SH) and give rise to the signal at 163.2 eV (164.4 eV), while the final

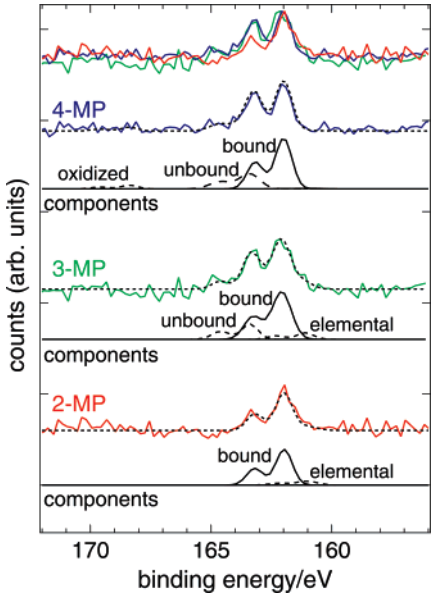

Figure 4. Sulfur 2p photoemission spectra for SAMs of each MP isomer prepared on Au(111) from pure EtOH solvent. The red, green, and blue spectra correspond to the experimental data recorded for SAMs prepared from each isomer of MP (2-MP, 3-MP, and 4-MP respectively). The experimental spectra are also overlaid with one another at the top of the graph for purposes of direct comparison. The best-fitting model for each experimental spectrum is displayed as an overlaying dotted black line. The components of each best-fitting model are observed below the corresponding experimental data. As an aid in distinguishing between the components of each best-fitting model, the 'bound' doublets are presented as a solid black line and the 'elemental', 'unbound', and 'oxidized' doublets are presented as dashed black lines.

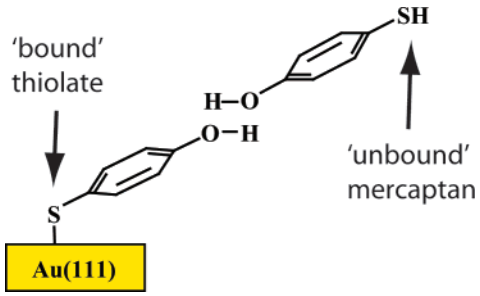

Figure 5. Schematic to illustrate the structure of a 4-MP-based surface dimer on Au(111) formed via hydrogen bonding between hydroxyl groups. The 'bound' monomer is attached to the underlying substrate via an Au−thiolate bond, while the 'unbound' monomer retains the full mercaptan (−SH) group.

resonance, observed in the region of 167.1 eV (168.3 eV), results from 'oxidized' sulfur. Any sample containing ≥10% oxidized sulfur was deemed to have degraded via exposure to atmospheric oxygen and, therefore, unsuitable for further study. Table 1 displays the integrated relative intensities of the S(2p) resonances for the MP SAMs. All intensities were corrected for photoelectron attenuation by the monolayer according to the methodology of Lamont et al.[49] Appropriate monolayer thicknesses were calculated using the colatitudal tilt angles obtained from NEXAFS analysis.

The S(2) PES spectra presented in Figure 4 demonstrate that 'bound' monomers predominate in MP SAMs prepared on Au(111). In fact, analysis of the S(2p) resonance intensities indicates that >70% of the organothiol monomers form an Au−S bond with the underlying substrate. By way of contrast,

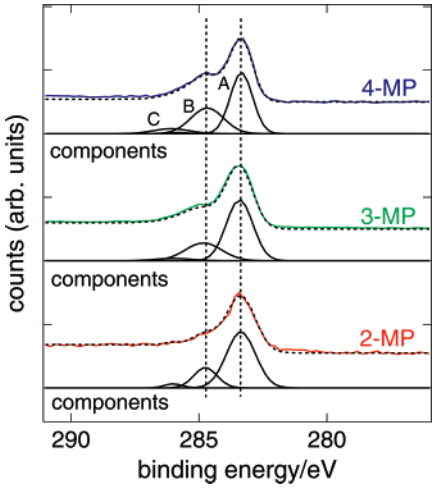

Figure 6. Carbon 1s photoemission spectra for SAMs of each MP isomer prepared on Au(111) from pure EtOH solvent. The best-fitting model for each experimental spectrum is displayed as an overlaying dotted black line. The components of each best-fitting model are offset below the corresponding experimental spectrum.

only a limited proportion of 'unbound' monomers are present within each monolayer (≤15%). Such low surface concentrations are desirable because the presence of 'unbound' monomers results in deviation from the idealized monolayer structure and surface functionality: the majority of the signal from unbound mercaptan is attributed to formation of hydrogen-bonded surface dimers of MP. Hydrogen bonding between a 'bound' and 'unbound' monomer (Figure 5) has the effect of burying the hydroxyl functional groups within a bilayer structure and exposing a mercaptan group at the SAM surface.

We note that the relative proportion of 'unbound' monomers within the MP monolayers is lower for the 2-derivative than either the 3- or 4-derivative. A reduced 'unbound' content implies that the hydroxyl groups within 2-MP SAMs are less accessible for dimerization via hydrogen bonding and, by extension, the stabilization of any ACC precipitate at the monolayer surface. Supporting evidence for this assignment is provided by static contact angles with water recorded for the MP monolayers, which are presented in Table 1. SAMs of 2-MP exhibit the largest contact angles ($\theta_s \approx 51°$) and, therefore, the least hydrophilic monolayer surfaces. As such, the hydroxyl groups of 2-MP are almost certainly buried deeper within the monolayer, thereby exposing more of the hydrophobic aryl ring at the sample surface. While buried within the monolayer, there exists the possibility that the hydroxyl groups of 'bound' 2-MP interact with the underlying substrate in a manner analogous to the carboxyl group of 2-mercaptobenzoic acid.[41] The result would be a bidentate bonding interaction between the 2-MP and the Au(111) surface via the mercaptan sulfur and the hydroxyl oxygen.

C(1s) PES provides an additional and complementary means with which to address the surface attachment and bonding of the MP monomers. Figure 6 displays representative C(1s) PES spectra recorded for SAMs prepared on Au(111) from each structural isomer of MP. Two resonances are readily identified in the spectra recorded for monolayers of each MP isomer. The first resonance (labeled A), observed at a binding energy of 283.4 eV, is attributed to the carbon atoms comprising the aryl ring, with the exception of the carbon bonded to the hydroxyl group. The second resonance (labeled B) arises from this

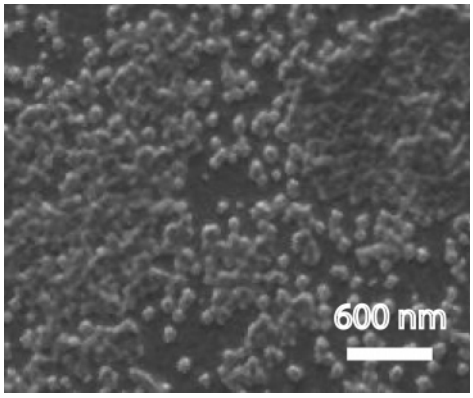

Figure 7. Characteristic SEM micrograph of ACC precipitate prepared on a 4-MP SAM on Au(111).

hydroxyl-bonded carbon and is shifted to a higher binding energy of 284.7 eV due to the inductive effect of the electronegative hydroxyl oxygen. The binding energy of the hydroxyl-bonded carbon peak is invariant between the isomers of MP, which indicates that the hydroxyl groups experience comparable chemical environments. Given that 'bound' monomers predominate within SAMs of 4-MP and due to constraints of their molecular orientation cannot interact with the underlying substrate via the hydroxyl group, this implies that the majority of 'bound' monomers of 2- and 3-MP are also unlikely to have formed hydroxyl−Au bonds. Modeling of the C(1s) spectra indicates the presence of a third, far less intense (<5% total signal), resonance (labeled C) at higher binding energy (~286.0 eV), which is attributed to a small amount of carbon contamination within the samples.

In summary, monomers of all three isomers of MP adopt well-defined molecular orientations within their respective SAMs on Au(111). Carbon *K*-edge NEXAFS measurements demonstrate that the aryl ring of each MP derivative has a statistically averaged tilt angle of ~60° with respect to the Au(111) surface normal, i.e., the monomers have a more prostrate than upright orientation. PES studies illustrate that all of the MP SAMs exhibit minimal dimerization via hydrogen bonding and, therefore, contain limited bilayer formation. In addition, the hydroxyl groups of the 3- and 4-derivatives are more accessible at the surface of their monolayers than for the 2-derivative. This extended characterization of the structure and bonding provides an excellent frame of reference with which to compare any morphological changes in the monolayers of MP following precipitation of ACC.

3.2. SAM Morphology and Bonding after Precipitation of ACC. In this section, we address the evolution in MP SAM morphology and bonding induced during precipitation of the amorphous mineral phase. SAMs prepared from 3- and 4-MP consistently stabilized the ACC precipitate at high surface coverages (~65%) and low thicknesses (≤100 nm), as illustrated by the scanning electron microscope (SEM) image presented in Figure 7. Both a high surface coverage and low thickness of the mineral are essential for purposes of characterizing the underlying SAM structure with carbon *K*-edge NEXAFS. In the first instance, a high surface coverage of ACC is necessary in order to accurately elucidate the orientation of monomers at the SAM/mineral interface. The NEXAFS signal represents an average over the region of the sample surface irradiated by the incident beam and, therefore, a convolution of all MP environments within the SAM. As a result, maximizing the surface coverage of $CaCO_3$ ensures that the signal is representative of monomers supporting the mineral phase rather than simply those in alternative environments, such as monomers occupying regions without coverage by ACC. In the second instance, thin precipitates (~100 nm) of ACC are desirable to limit X-ray attenuation by the mineral layer.[50] Coupled with an appropriate surface coverage of ACC for escape by sufficient secondary electrons,[51,52] this allows for TEY measurements of the MP monolayer.

Monolayers prepared from 2-MP were less reliable in stabilizing the ACC precipitate at high surface coverage, potentially due to the comparative inaccessibility of the hydroxyl groups with respect to 3- and 4-MP: $CaCO_3$ crystallization occurred extensively on the 2-MP surfaces within the time frame required to yield ~65% surface coverage of ACC on the 3- and 4-MP monolayers. In fact, the degree of crystallization was such that it was not possible to obtain a 2-MP surface with ≥65% coverage of ACC or, indeed, without a high proportion of $CaCO_3$ crystallites on the SAM. SEM imaging of the $CaCO_3$ crystallites also indicated no preferential crystallographic plane of calcite nucleation on the 2-MP SAMs. As a consequence, ACC/2-MP samples were excluded from study with carbon *K*-edge NEXAFS and experiments were focused upon the ACC/3-MP and ACC/4-MP systems. Figure 8a and b displays representative NEXAFS spectra recorded for ACC on SAMs of 3-MP and 4-MP, respectively. As anticipated, each spectrum contains the series of resonances observed for 3- and 4-MP monolayers in the absence of ACC precipitate. An additional resonance, observed at 290.5 eV, is attributed to the π^* transition for the CO_3^{2-} ion of the mineral phase. The CO_3^{2-} π^* resonance is resolved in energy with respect to the π^* resonances of the aryl ring and also arises at a higher incident photon energy. Hence, the aryl ring π^* resonances are readily resolved from the ACC signal for purposes of assigning molecular orientation within the SAM. This represents a distinct advantage over any ACC/OH-terminated alkanethiol SAM system for purposes of obtaining an accurate assignment of monomer orientation following formation of the $CaCO_3$ phase. All of the NEXAFS resonances from an OH-terminated alkanethiol monolayer would be convoluted with the ACC signal, necessitating extensive modeling to separate the spectral contribution from each phase and introducing a substantial source of error in the measurement of molecular orientation. We observe that the CO_3^{2-} π^* resonance exhibits a minimal angular dependence in Figure 8a and b, which is consistent with formation of an amorphous $CaCO_3$ phase.

A striking contrast is observed between the difference spectra recorded before (Figure 1b and c) and after (Figure 8a and b) ACC precipitation. The angular dependence of the aryl ring π^* resonances is severely reduced following formation of ACC on both the 3- and 4-MP monolayers. Two explanations can be proposed for this phenomenon. Significantly, both correspond to a profound change in the monomer orientation after formation of the ACC deposit: (1) The loss of angular dependence could arise in the event that the SAM is composed of monomers with a statistically averaged random distribution of molecular orientations, i.e., a disordered monolayer (Figure 9). For a monolayer containing extensive static disorder, the distribution of molecular orientations would result in comparable π^* resonance intensities

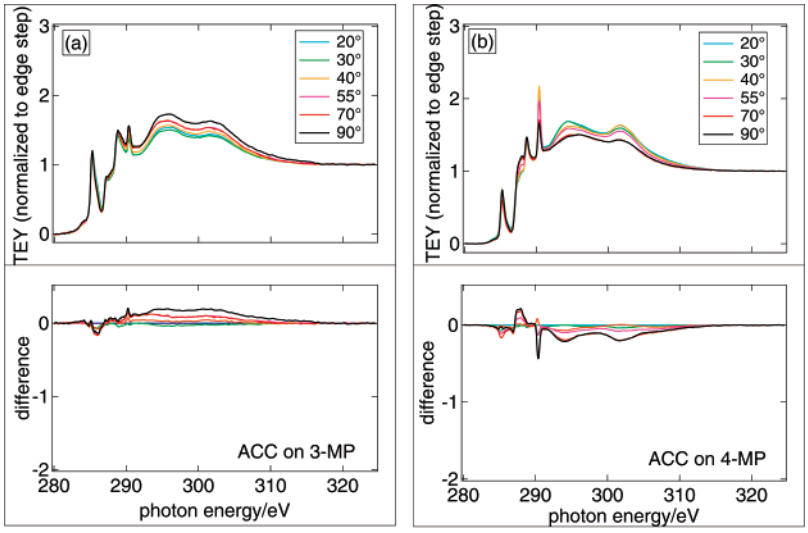

Figure 8. Normalized carbon *K*-edge NEXAFS spectra recorded in the TEY mode for samples of ACC on (a) a 3-MP SAM and (b) a 4-MP SAM prepared on Au(111) substrates.

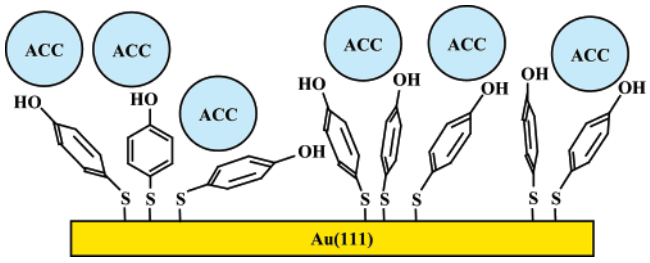

Figure 9. Schematic to illustrate an ACC/4-MP system in which the SAM is comprised of monomers with a random distribution of orientations. Note that the ACC particles are not drawn to scale and are, in fact, orders of magnitude larger than the MP monomers.

at all angles of incidence between the axis of the X-ray beam and the surface of the experimental sample. This loss of angular dependence would be illustrated by a substantial reduction in magnitude of the aryl ring π^* difference features. (2) Precipitation of ACC could have induced a molecular reorientation in which the tilt angle of the TDM vector of the π^* orbital changes from ~30° to close to the magic angle, 54.7°. A reorientation of this variety would correspond to the tilt angle of the aryl ring changing from ~60° to close to 35.3° with respect to the surface normal. In this instance, the reduction in magnitude of the difference features would arise because the π^* resonance intensities become increasingly similar (and, ultimately, equal) as the TDM vector approaches the magic angle.

Linear regression analysis of the aryl ring π^* resonance intensities does not allow for direct assignment of either mode of structural reorder within the MP SAMs: the colatitudal tilt angles obtained for the TDM vector of the π^* orbital of 3- and 4-MP, 52° and 55°, respectively, reside within experimental error of the magic angle, which would be consistent with either the disordered monolayer of (1) or the molecular reorientation of (2). Even so, the probability that molecular reorientation in the 3- and 4-MP SAMs results in the monomers adopting identical tilt angles at the magic angle is extremely small. Therefore, it is inferred that precipitation of ACC results in a statistically averaged disordering of the MP monomers.

Some consideration must be given to the possible effects on monomer orientation caused by drying the ACC/MP SAM samples prior to conducting the carbon *K*-edge NEXAFS

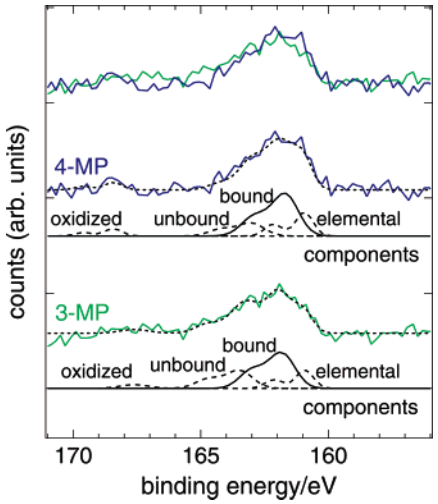

Figure 10. Sulfur 2p photoemission spectra for SAMs of 3- and 4-MP following precipitation of ACC. The experimental spectra, best-fitting model spectra, and components of the best-fitting models are displayed according to the scheme described in Figure 4.

measurements. In the absence of ACC, our data demonstrates that the SAM monomers exhibit well-defined orientations following the drying process. Even so, ACC is a hydrated phase and could undergo dehydration during drying of the ACC/MP SAM samples, which would result in shrinkage of the ACC particles and, in principle, lead to strain within the MP monolayer. Analysis of the potential magnitude of this effect indicates, however, that it could only account for a minor fraction (see Supporting Information) of the molecular disorder necessary to induce the loss of angular dependence observed for the aryl π^* resonance in the NEXAFS spectra.

Figure 10 contains characteristic S2p PES spectra recorded for the ACC/3-MP and ACC/4-MP systems. Accompanying integrated relative intensities for the S2p resonances, obtained as an average over spectra from multiple samples, are contained in Table 1. Photoelectrons emitted from sulfur atoms of the MP monomers beneath the ACC minimally contribute to the S(2p) PES spectra due to attenuation by the mineral phase (the photoelectron attenuation length in ACC is <10 nm). As a consequence, the S(2p) signals arise overwhelmingly from

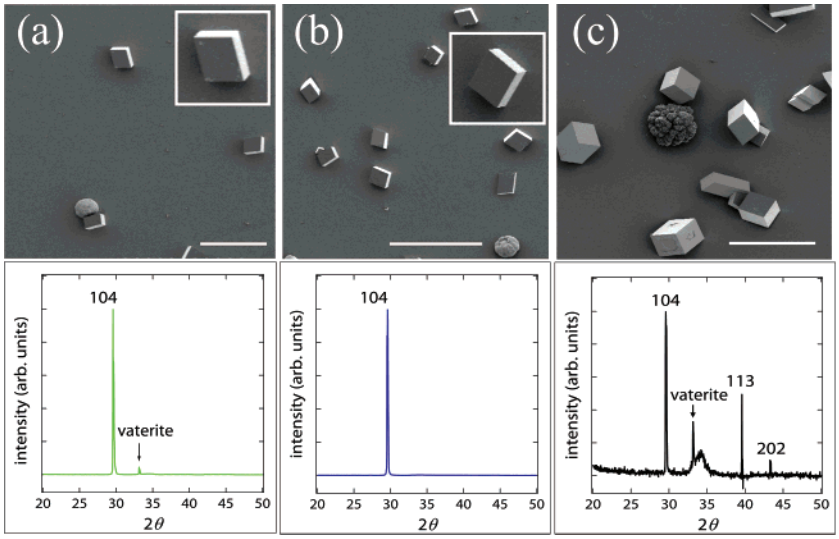

Figure 11. SEM micrographs of crystalline $CaCO_3$ growth on (a) a 3-MP SAM, (b) a 4-MP SAM, and (c) a flame-annealed Au substrate. All scale bars are 100 μm. Higher magnification images of representative calcite crystals from the 3-MP and 4-MP SAMs are inset in a and b, respectively. Each SEM image is accompanied by a representative XRD pattern for the sample of interest.

regions of the SAM that do not support any ACC and exhibit a corresponding reduction in S/N relative to the spectra obtained from the as-prepared SAMs (Figure 4). It is significant, however, that analysis of the spectra indicates a limited amount of SAM degradation in these uncovered regions due to prolonged exposure in aqueous solution because one would anticipate comparable behavior in the regions located beneath the mineral. 'Bound' monomers continue to predominate within the monolayers (~60%), although there is a small increase (~5%) in the 'unbound' contribution, which is attributed to solvent-mediated organothiol desorption from the Au substrate. An accompanying ~10% increase in the 'elemental' signal could indicate monolayer degradation via fragmentation of the Au−S bond or sulfur contamination from the Ca^{2+}-bearing solution.

In summary, the 3- and 4-MP SAMs contain a statistically averaged random distribution of monomer orientations following precipitation of ACC. Despite the structural disorder within the SAMs, the majority of the monomers remain attached to the underlying Au(111) substrate via an Au−thiolate bond.

3.3. Morphology and Orientation of Crystals Nucleated after ACC Precipitation. We now examine the degree to which these disordered MP SAMs induce calcite nucleation on a specific face. The carbon *K*-edge NEXAFS measurements provide compelling evidence that SAMs prepared from the isomers of MP do not act as rigid platforms for $CaCO_3$ nucleation and growth. In conjunction with the S(2p) PES measurements, they illustrate that there is substantial evolution in the monolayer structure and bonding during the process of ACC precipitation, which occurs even before the onset of mineral crystallization. Given that the MP monolayers adopt disordered structures beneath ACC, the precursor to crystalline $CaCO_3$ formation, one must also address whether they are capable of inducing crystallographic plane-specific nucleation of calcite with the control exhibited by ω-substituted alkanethiol SAMs. In this regard, SEM and XRD measurements provide the means with which to characterize the phase and orientation of crystalline $CaCO_3$ that eventually forms through replacement of ACC on monolayers of MP. Figure 11a and b displays representative SEM micrographs and XRD spectra collected following crystallization of $CaCO_3$ on SAMs of 3- and 4-MP, respectively. Two polymorphs of crystalline $CaCO_3$, calcite and vaterite, are evident in the SEM images and were observed on the MP SAM surfaces at a ratio of ~80:20. A prevalence of calcite is consistent with reported studies of $CaCO_3$ crystallization on Langmuir monolayers[6] and SAMs on Au and Ag substrates[16] prepared from hydroxyl-terminated alkanethiol monomers.

A highly uniform crystallographic orientation is also apparent among the calcite rhombohedra formed on the 3- and 4-MP SAMs. Geometrical analysis of crystals imaged during the SEM studies indicates that calcite preferentially nucleates on the (104) face (~70%). The corresponding XRD spectra presented in Figure 11a and b provide supporting evidence for the assignment of face-selective nucleation on the (104) plane of calcite. This result is consistent with previous work showing preferential expression of calcite on the (104) face for hydroxyl-terminated alkanethiol SAMs prepared on Au.[16] Thus, we conclude that monolayers of 3- and 4-MP bring about the controlled nucleation of calcite from ACC with well-defined orientation despite disordering during precipitation of the ACC precursor.

3.4. Pathway of Transformation from ACC to Crystalline $CaCO_3$. SEM micrographs collected for composite ACC−calcite films allow identification of the pathway of $CaCO_3$ transformation in the $CaCO_3$/MP SAM systems. The composite films are created by removing the MP SAMs from solution and drying during the transformation process. As the SEM micrograph in Figure 12 shows, once a calcite nucleus forms, a ring of ACC particles surrounding the calcite crystal disappears. This result demonstrates that the transformation process occurs via ACC dissolution during calcite formation.

4. Discussion

4.1. Importance of SAM and Substrate in Directing Crystal Orientation. A common paradigm for interpreting observations of orientation control during nucleation, i.e., templating, is that there is a stereochemical or epitaxial match between headgroups of the SAM and solute ions in the mineral phase.[20] In the case of OH-terminated SAMs, numerous objections can be raised. The first is that there are no specific chemical interactions between the monolayer and the crystal

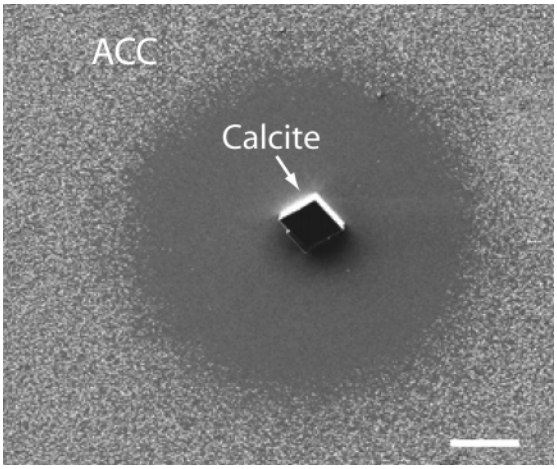

Figure 12. SEM micrograph of a (104) calcite rhombohedron during the conversion from ACC to crystalline $CaCO_3$. The zone surrounding the calcite crystal is entirely depleted of ACC. The scale bar is 10 μm.

face during $CaCO_3$ crystallization on hydroxyl-terminated films, as proposed by Mann et al.[6] The preferential alignment of calcite is instead attributed to surface tension forces. However, this condition would not preclude monolayer control over the face of nucleation because the surface tension would still be dependent upon the morphology and composition of the SAM. In addition, the surface tension is directly related to the interfacial energy, which, along with supersaturation, is the single most important factor in determining the rate of nucleation. This point will be discussed further below.

Second, since the (104) face is the one expressed on calcite crystals nucleated in bulk solution, one might argue that the nucleating phase of $CaCO_3$ is not in direct contact with the surface of the underlying monolayer but is separated by a thin layer of water between the two. In this event, the mode of crystallization could be independent of the hydroxyl-terminated monolayer and more closely comparable to nucleation in bulk solution because the incipient nuclei will be surrounded by solvent molecules. Experimental evidence conflicts with this hypothesis. If $CaCO_3$ crystallization is unaffected by the monolayer and occurs in a similar environment to bulk solution, different hydroxyl-terminated surfaces should yield crystals with the same orientations or distributions of orientations under identical experimental conditions. Crystallization of $CaCO_3$ on glass substrates, which are known to provide hydroxyl-terminated (albeit comparatively rough) surfaces, produced a largely random distribution of calcite orientations rather than the preferential ordering observed for MP SAMs (Figure 13a). Furthermore, Aizenberg et al. reported that calcite crystals formed on monolayers of the same hydroxyl-terminated alkanethiol (11-mercapto-1-undecanol) prepared on different noble-metal substrates (Ag and Au) exhibit well-defined but distinct crystallographic orientations (nucleation on the (103) and (104) planes, respectively).[16] Therefore, even if a water layer separates the monolayer from the incipient nuclei, the experimental evidence shows that some combinations of SAM and substrate are still able to direct calcite nucleation.

Finally, given that calcite nucleation is favored on the (104) plane for three different hydroxyl-terminated monolayers prepared on Au(111) (i.e., 3-MP, 4-MP, and 11-mercapto-1-undecanol), we must consider whether control over mineral formation is a function of only the underlying metal substrate rather than the entire monolayer/substrate system. SEM and XRD measurements of calcite crystallization on flame-annealed Au(111) substrates address this concern by demonstrating that a random distribution of crystal orientations results in the absence of any organothiol SAM (Figure 11c). Aizenberg et al. reported comparable results for the nucleation and growth of $CaCO_3$ on bare Au and Ag surfaces under similar experimental conditions.[16] Our current results also illustrate that there is no control over orientation during nucleation on the 2-MP monolayers (Figure 12b). Hence, it is apparent that the hydroxyl-terminated MP monolayers are themselves critical components for directed nucleation of $CaCO_3$ in these systems.

On the basis of the results presented here as well as the previous observations described above, we conclude that certain combinations of OH-terminated SAMs and substrates play a determining role in directing the orientation of crystal nuclei during the transformation of ACC to calcite. Moreover, this conclusion holds even when the monolayers have lost their orientational order prior to the transformation.

4.2. Mechanism of Control over Orientation. The driving force for ACC dissolution during calcite formation is the high solubility of ACC, which is reported to be ~100 times that of calcite.[53] As soon as a calcite crystal appears in the ACC film, the surrounding solution becomes highly undersaturated with respect to ACC, thereby causing it to dissolve. As the solute ions from the dissolving ACC are transferred to the growing crystal, an ACC-free region rapidly spreads outward (Figure 12). A movie of this process can be found in the Supporting Information.

The rate of nucleation of a new mineral phase is governed by the magnitude of the free energy barrier associated with the transformation. This free energy barrier arises from the excess free energy of the mineral phase due to the large fraction of molecules that resides in a poorly coordinated state at the surface of the microscopic nucleus. Thus, the single most important material parameter determining the nucleation rate J_n is the surface free energy α. Indeed, the rate of nucleation is exponentially dependent on the third power of α through[54,55]

$$J_n = A \exp\left(\frac{-B\alpha^3}{\sigma^2}\right) \tag{5}$$

where A and B are constants that depend on many parameters and σ is the supersaturation with respect to the solid phase. Thus, the nucleation rate is not necessarily maximum for the solid phase for which the solution is most highly supersaturated but instead may be maximum for the one with the lowest surface free energy.[56] (This is the basis of the Ostwald−Lussac rule[57] and the reason why ACC forms before calcite in these systems despite the fact that the solubility constant of ACC is so much larger than that of calcite.) However, in all of the experiments discussed here, calcite forms out of ACC, which means that the concentration of the solution and therefore the supersaturation with respect to calcite at the time of the transformation is always the same; it is defined by the solubility of ACC. Consequently, the only differences that can lead to preferential

(54) Nielsen, A. E. *Kinetics of Precipitation*; Pergamon: New York, 1964.
(55) Abraham, F. F. *Homogeneous Nucleation Theory*; Academic Press: New York, 1974.
(56) Duffy, D. M.; Harding, J. H. *J. Mater. Chem.* **2002**, *12*, 3419.
(57) Nancollas, G. H. *Biological Mineralization and Demineralization. Life Sciences Research Report*; Springer-Verlag: New York, 1982.

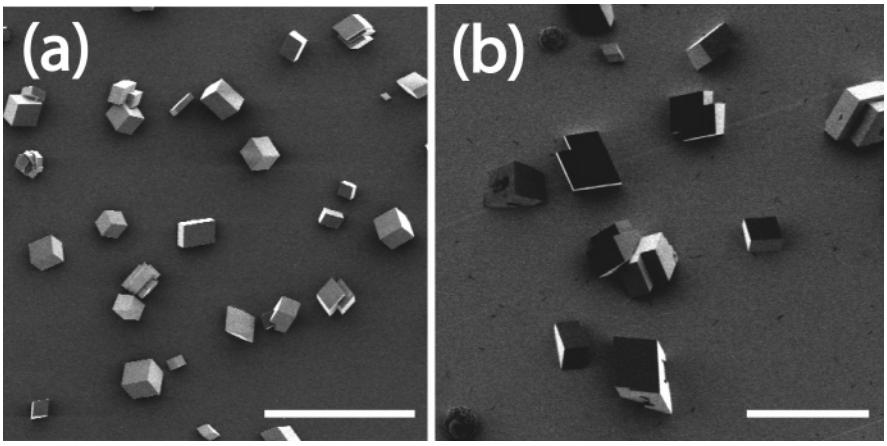

Figure 13. SEM micrographs of crystalline $CaCO_3$ growth on (a) glass and (b) a 2-MP SAM prepared on Au(111). The scale bars are 100 μm.

nucleation are to be found in α. Introduction of a substrate can alter α because it introduces an interface that differs from the crystal−solution interface. The value of α in bulk solution is replaced with[58,59]

$$\alpha = \alpha_{lc}\{1 - (\alpha_{ls} - \alpha_{sc})/2\alpha_{lc}\} \quad (6)$$

α_{lc}, α_{ls}, and α_{sc} are the interfacial free energies for the liquid−crystal, liquid−substrate, and substrate−crystal interfaces, respectively. The term in the brackets is always less than 1 provided the free energy of the crystal−substrate interface is less than that of the substrate−liquid interface. For the case of calcite nucleation after ACC, all terms in eq 6 are identical except for α_{sc}. The consequence of eqs 5 and 6 is that if there is a particular crystal face for which α_{sc} is minimized, the probability of nucleation on that face is dramatically enhanced. However, this analysis assumes nothing about chemical interactions. While it is evident that stereochemical and epitaxial relationships between surfaces and crystals can drive anisotropic energy minimization, they are not required. Any interactions that provide a more favorable electrostatic or bonding environment will do.

An unequivocal assignment of the mechanism for monolayer-mediated anisotropic reduction of the interfacial energy in the calcite/OH-SAM-on-Au system cannot be obtained from the structural information provided by this study alone. Nevertheless, three prospective modes of monolayer control are consistent with the presence of a statistically averaged random distribution of molecular orientations in the SAM: First, the interfacial energy of the calcite (104) plane may be minimized due to electrostatic or other nonspecific interactions when placed in contact with the disordered, OH-terminated, surface. This appears to be unlikely, however, given the absence of preferential ordering for nucleation on the disordered, OH-terminated, surfaces of glass substrates and the substrate-dependent face of nucleation observed for calcite crystallization on 11-mercapto-1-undecanol SAMs.[16]

Second, the anisotropic reduction in the interfacial energy could be driven by specific interactions that are favored by certain stereochemical or epitaxial relationships between the (104) face and OH-terminated SAMs. In this case, a cooperative interaction between the organic and inorganic phases leads to local reordering of the SAM during the nucleation stage. This reordering is made possible by the inherent thermal fluctuations of the organothiol molecules and the high rates of attachment and detachment events that occur at solution/mineral surfaces. In other words, the crystal and monolayer template one another. Significantly, it has been proposed that a degree of structural flexibility in the organic monolayer is an important feature in other examples of templated crystallization.[36,60]

Finally, even though the SAM is disordered, limited regions of well-defined molecular order and packing could exist within the disordered monolayer and act as templates for crystal growth. The presence of ordered regions remains a possibility because the assignment of monolayer disorder is based upon a statistical average over the entire sample surface. This is particularly significant because only extremely small areas of order would be required to induce a templating effect. Under the experimental conditions employed in the crystallization of calcite, it is estimated that the critical radius, r_c,[59] falls within $10 \leq r_c \leq 100$ Å. Assuming that the MP SAMs adopt comparable packing arrangements to monolayers prepared from similar, aryl-ring based, organothiol monomers,[61,62] the footprint of the incipient nucleus could cover as little as ~15 MP monomers during the process of templating.

The phenomenon of ordered crystal formation following disordering of the MP monolayer structure provides an interesting comparison with the crystallization of calcite on carboxyl-terminated alkanethiol SAMs. In contrast to hydroxyl-terminated monolayers, the face-selective nucleation induced on monolayers with carboxyl end-group functionality has been directly attributed to specific chemical interactions at the SAM/crystal interface.[20] Moreover, in studies reported to date, ACC is only stable on carboxyl-terminated films in the presence of an additive, such as PAA or poly(aspartic acid). Despite evident differences in the behavior of monolayers with hydroxyl and carboxyl end-group functionality during $CaCO_3$ crystallization, structural disorder within the SAM is a feature of both systems. For example, X-ray scattering studies provide evidence of

(58) Mullin, J. W. *Crystallization*, 3rd ed.; Butterworths: Markham, ON, Canada, 1992
(59) Kashchiev, D. *Nucleation: Basic Theory with Applications*; Butterworths: Markham, ON, Canada, 1999
(60) Cooper, S. J.; Sessions, R. B.; Lubetkin, S. D. *J. Am. Chem. Soc.* **1998**, *120*, 2090.
(61) Azzam, W.; Cyganik, P.; Witte, G.; Buck, M.; Wöll, C. *Langmuir* **2003**, *19*, 8262.
(62) Cyganik, P.; Buck, M.; Azzam, W.; Wöll, C. *J. Phys. Chem. B* **2004**, *108*, 4989.

disorder in carboxyl-terminated alkanethiol SAMs following crystallization of Mg-incorporated calcite.[24] Recent reports also indicate that carboxyl-terminated alkanethiol SAMs prepared in pure ethanol solvent, an established and almost universally accepted protocol, contain a substantial degree of molecular disorder,[40,63−65] which includes a random distribution of end-group orientations.[40] In addition, S(2p) PES studies provide evidence for considerable dimerization between 'bound' and 'unbound' monomers via hydrogen bonding of the carboxyl groups. Hence, even in this canonical case of crystal templating, the nucleation of calcite on well-defined crystallographic planes is directed by a monolayer that is characterized by disordered end groups and monomer dimerization at the outset.

5. Conclusions

In summary, when exposed to calcium carbonate solutions formed through CO_2 diffusion into calcium chloride solutions, SAMs initially containing monomers of 3- or 4-MP with well-defined orientations become substantially disordered. In addition, the SAMs become covered with a film of ACC particles, each $\leq$100 nm in diameter. Although the ACC films are stable in solution for periods of a few hours, they eventually transform into discrete crystals of $CaCO_3$ via what is clearly a dissolution−reprecipitation reaction. The resulting crystals are predominantly calcite, although some vaterite ($\leq$20%) is also present. In the case of the 3- and 4-MP monolayers, the plane of nucleation for the calcite crystals exhibits a high degree of uniformity with over 70% nucleating on the (104) face. Comparison with other systems, including OH-terminated amorphous SiO_2 surfaces, bare Au(111) and SAMs of OH-terminated organothiols on Ag and Au substrates demonstrate that the presence of the SAM is crucial for directing nucleation, despite any inherent structural disorder. While residual order at short length scales (<10 nm) may be responsible for the apparent anisotropic reduction in interfacial energy associated with the preferential nucleation plane, a cooperative interaction that results in reordering of the monolayer during nucleation is equally probable. In this instance, the crystal and monolayer would template one another. Direct comparison indicates that a comparable process could occur during calcite nucleation on carboxyl-terminated alkanethiol SAMs prepared on Au. Hence, this evolution may define the general sequence of events associated with templated growth of calcite following formation of ACC, a process that is increasingly viewed as a common phenomenon in biomineralizing systems.

Acknowledgment. This work was supported by the Divisions of Chemical, Biological and Geochemical Sciences and Materials Science, Office of Basic Energy Science, and the U.S. National Institutes of Health grant DK61673 and performed under the auspices of the U.S. DoE by LLNL under contract W-7405-ENG-48. Portions of this research were carried out at the Stanford Synchrotron Radiation Laboratory, a national user facility operated by Stanford University on behalf of the U.S. Department of Energy, Office of Basic Energy Sciences. The authors thank the SSRL staff, particularly Dan Brehmer and Curtis Troxel, for their assistance during the course of these experiments. In addition, the authors thank Cheng Saw for collection of the XRD spectra presented in this manuscript.

Supporting Information Available: Extended experimental details for ACC precipitation and $CaCO_3$ crystallization; linear regression analysis of carbon *K*-edge NEXAFS spectral data; possible combinations of tilt and twist angles for the isomers of MP in their respective, as prepared, SAMs; additional discussion of possible ACC dehydration and the resulting effects upon the MP SAM structure; and a movie of the dissolution−reprecipitation reaction for calcite crystallization from ACC on a plastic substrate. This material is available free of charge via the Internet at http://pubs.acs.org.

JA071535W

(63) Arnold, R.; Azzam, W.; Terfort, A.; Wöll, C. *Langmuir* **2002**, *18*, 3980.
(64) Dannenberger, O.; Weiss, K.; Himmel, H. J.; Jager, B.; Buck, M.; Wöll, C. *Thin Solid Films* **1997**, *307*, 183.
(65) Wang, H.; Chen, S.; Li, L.; Jiang, S. *Langmuir* **2005**, *21*, 2633.